Front Waves in the NO + NH_3 Reaction on Pt{100}

I. M. Irurzun,† E. E. Mola,† and R. Imbihl‡

Instituto de Investigaciones Fisicoquímicas Teóricas y Aplicadas (INIFTA), Argentina, and Institut für Physikalische Chemie und Elektrochemie, Universität Hannover, Germany

Received: December 27, 2006; In Final Form: February 26, 2007

In the present work, we spatially extended a brand new kinetic mechanism of the NO + NH_3 reaction on Pt{100} to simulate the experimentally observed spatiotemporal traveling waves. The kinetic mechanism developed by Irurzun, Mola, and Imbihl (IMI model) improves the former model developed by Lombardo, Fink, and Imbihl (LFI model) by replacing several elementary steps to take into account experimental evidence published since the LFI model appeared. The IMI model achieves a better agreement with the experimentally observed dependence of the oscillation period on temperature. In the present work, the IMI model is extended by considering Fickean diffusion and coupling via the gas phase. *Traveling waves propagating across the surface are obtained at realistic values of temperature and partial pressure.* A transition from amplitude to phase waves is observed, induced either by temperature or by the gas global coupling strength. *The traveling waves simulated in the present work are not associated with fixed defects, in agreement with experimental evidence of spiral centers capable of moving on the surface.* Also, the IMI model adequately predicts the presence of macroscopic oscillations in the partial pressures of the reactants coexisting with front wave patterns on the surface.

1. Introduction

The dynamic behavior of the catalytic reduction of NO shows phenomena such as multiple steady states and temporal oscillations in the rate of the reaction or in the partial pressures of the reactants.[1−3] Under ultrahigh vacuum conditions, the temporal oscillations exhibited by the NO + NH_3 reaction on single-crystal metal surfaces are associated with the existence of a reversible phase transition in the crystalline structure of the metal surface induced by the adsorption of NO upon a critical value.[3−7]

Kinetic oscillations in the NO + NH_3 reaction on Pt{100} have been studied extensively, and the experimental conditions under which these oscillations arise have been reported. In addition, the experimental temperature and partial pressure dependence of the oscillatory period has been determined, and based on this information, kinetic models have been developed in the mean-field approximation.

The model developed by Lombardo, Fink, and Imbihl (LFI model) represents a realistic kinetic model of this reaction, capable of reproducing temporal oscillations, though the agreement with the experiment is rather poor. Further improvements were introduced by King and co-workers mainly considering the experimentally observed coverage-dependent sticking probabilities and desorption activation energy.[9−12]

Recently, the LFI model has been additionally improved by Irurzun, Mola, and Imbihl (IMI model).[13] The IMI model takes into consideration recent experimental and theoretical evidence showing that the dominant reaction pathway leading to NH_3 decomposition is via direct abstraction of an H atom from adsorbed ammonia via adsorbed oxygen or OH.[14] The model also considers the influence of dynamic defects on the kinetic behavior of the reaction, that is, defects created during the $1 \times 1 \rightarrow$ hex phase transition. The important role of such defects has been shown by Imbihl and co-workers in periodic forcing experiments in the CO + NO reaction on Pt{100}.[15] From these studies, the activation energy for the annealing process could be determined.[13]

The IMI model achieved a significant improvement in the kinetic behavior, as compared with experimental information, mainly in the dependence of the oscillatory period on temperature

Simultaneously, the LFI model has been adiabatically reduced,[16] spatially extended with Fickean diffusion, and numerically studied in 1D and 2D.[17,18] Though simulation showed a variety of patterns, the overall agreement with the experiment is poor. *In particular, the dependence on the temperature is in reverse order compared to the experimental information.*[17] To justify this disagreement, it has been argued that the gas global coupling may account for the observed discrepancies. More recently, the site-blocking effects of coadsorbates on diffusing species have been included in the LFI model. Also, macroscopic surface defects fixed on the catalyst have been taken into account.[19] *The existence of traveling waves was initially ascribed to these two modifications, although experimental evidence had been presented previously supporting the existence of wave sources capable of moving on the surface.*[20]

In the present work, we spatially extend the IMI model and show that it predicts the existence of traveling waves at realistic values of temperatures and partial pressures. We argue that this success is due to the improvement of the kinetic behavior of the model. The waves are not associated with fixed defects, in agreement with the experimental evidence.[20] Global coupling via the gas phase is also introduced, and we show that traveling patterns can coexist with macroscopic partial pressure fluctuations as observed in experiments.

* Author to whom correspondence should be submitted. Postal Address: Casilla Correo 314, (1900) La Plata, República Argentina. E-mail: eemola@inifta.unlp.edu.ar.

† INIFTA.

‡ Universität Hannover.

10.1021/jp0689666 CCC: $37.00
Published on Web 04/07/2007

2. Model

The IMI model for the NO + NH_3 reaction on Pt{100} is an improved mechanism of the former LFI model where several elementary steps have been modified to take into account experimental evidence published since the LFI model appeared.[9−13] It consists of a set of eight ordinary differential equations (ODEs) describing the time evolution of chemical species on the metal surface in the mean-field approximation, as well as the fraction of the surface in 1 × 1 phase, and the fraction of surface defects created during the phase transition and destroyed by annealing.

$$\frac{d}{dt}\theta_{NO}^{1\times1} = F_{NO}p_{NO}(\theta_{1\times1} - \theta_{NO}^{1\times1} - 4\theta_{NH_3}^{1\times1}) - k_1\theta_{NO}^{1\times1} - k_2\frac{\theta_{NO}^{1\times1}\,\theta_{empty}^{1\times1}}{\theta_{1\times1}} + k_3\frac{\theta_{NO}^{hex}(\theta_{1\times1} - \theta_{NO}^{1\times1} - 4\theta_{NH_3}^{1\times1})}{\theta_{1\times1}\theta_{hex}} - k_{12}\frac{\theta_{NO}^{1\times1}(\theta_{hex} - \theta_{NO}^{hex})}{\theta_{1\times1}\theta_{hex}} \quad (1)$$

$$\frac{d}{dt}\theta_{NO}^{hex} = F_{NO}p_{NO}(\theta_{hex} - \theta_{NO}^{hex}) - k_4\theta_{NO}^{hex} + k_3\frac{\theta_{NO}^{hex}(\theta_{1\times1} - \theta_{NO}^{1\times1} - 4\theta_{NH_3}^{1\times1})}{\theta_{1\times1}\theta_{hex}} + k_{12}\frac{\theta_{NO}^{1\times1}(\theta_{hex} - \theta_{NO}^{hex})}{\theta_{1\times1}\theta_{hex}} \quad (2)$$

$$\frac{d}{dt}\theta_{NH_3}^{1\times1} = F_{NH_3}p_{NH_3}(\theta_{1\times1} - 3\theta_{NH_3}^{1\times1} - 1.6\theta_{NO}^{1\times1}) - k_5\theta_{NH_3}^{1\times1} - k_6\frac{\theta_{NH_3}^{1\times1}\,\theta_{O}^{1\times1}}{\theta_{1\times1}} + k_7\frac{\theta_{N}^{1\times1}\,\theta_{H}^{1\times1}}{\theta_{1\times1}} \quad (3)$$

$$\frac{d}{dt}\theta_{O}^{1\times1} = k_2\frac{\theta_{NO}^{1\times1}\,\theta_{empty}^{1\times1}}{\theta_{1\times1}} - k_8\frac{\theta_{O}^{1\times1}\,\theta_{H}^{1\times1}}{\theta_{1\times1}} - k_6\frac{\theta_{NH_3}^{1\times1}\,\theta_{O}^{1\times1}}{\theta_{1\times1}} \quad (4)$$

$$\frac{d}{dt}\theta_{N}^{1\times1} = k_2\frac{\theta_{NO}^{1\times1}\,\theta_{empty}^{1\times1}}{\theta_{1\times1}} + k_6\frac{\theta_{NH_3}^{1\times1}\,\theta_{O}^{1\times1}}{\theta_{1\times1}} - k_7\frac{\theta_{N}^{1\times1}\,\theta_{H}^{1\times1}}{\theta_{1\times1}} - k_9\frac{(\theta_{N}^{1\times1})^2}{\theta_{1\times1}} \quad (5)$$

$$\frac{d}{dt}\theta_{H}^{1\times1} = k_6\frac{\theta_{NH_3}^{1\times1}\,\theta_{O}^{1\times1}}{\theta_{1\times1}} - 3k_7\frac{\theta_{N}^{1\times1}\,\theta_{H}^{1\times1}}{\theta_{1\times1}} - 2k_8\frac{\theta_{O}^{1\times1}\,\theta_{H}^{1\times1}}{\theta_{1\times1}} - k_{10}\frac{(\theta_{H}^{1\times1})^2}{\theta_{1\times1}}$$

$$\frac{d}{dt}\theta_{1\times1} = \begin{cases} \dfrac{\left(\frac{d}{dt}\theta_{NO}^{1\times1}\right)}{\theta_{grow}^{1\times1}} \rightarrow \text{if } \left[\left(\frac{d}{dt}\theta_{NO}^{1\times1} > 0\right) \text{and } (\theta_{NO}^{1\times1} \geq \theta_{grow}^{1\times1}\theta_{1\times1}) \right. \\ \qquad \left. \text{and } (\theta_{1\times1} < (1 - \theta_{def}^{1\times1})) \text{ and } (c > 1)\right] \\ -k_{11}(\theta_{1\times1} - \theta_{def}^{hex})(1 - c) \rightarrow \\ \qquad \text{if } [(\theta_{1\times1} \geq \theta_{def}^{hex}) \text{ and } (c \leq 1)] \\ 0 \rightarrow \text{otherwise} \end{cases} \quad (6)$$

$$\frac{d}{dt}\theta_{def} = k_{13}\left|\frac{d\theta_{1\times1}}{dt}\right| - k_{14}\theta_{def} \quad (7)$$

The coverages of the adsorbed species are normalized by the total number of sites; that is, the local coverages in hex and 1 × 1 phases can be obtained by dividing the normalized coverages by θ_{hex} and $\theta_{1\times1}$, respectively, and the relation $\theta_{hex} + \theta_{1\times1} = 1$ is valid. This formulation neglects that the two surface phases differ by about 16% in the density of surface atoms. Simple Langmuirian kinetics was assumed for adsorption by setting the adsorption rate proportional to the number of vacant sites. The prefactors $F_x p_x$ (x = NO,NH_3) are the adsorption fluxes that are the product of the impingement rates of the gas particles times the initial sticking coefficients s_x^0, and $s^0 = 1$ was set for all gases.

The inhibitory effect of adsorbates on NO dissociation and the stabilizing effect on the adsorbates for the 1 × 1 phase in eqs 4 and 5 are considered as in the LFI model and are given by[3,16,17]

$$\theta_{empty}^{1\times1} = \max\left[\left(\theta_{1\times1} - \frac{\theta_{NO}^{1\times1}}{\theta_{NO}^{inh}} - \frac{\theta_{O}^{1\times1}}{\theta_{O}^{inh}}\right), 0\right] + \max[(\theta_{def}^{1\times1} - \theta_{O}^{1\times1}), 0] \quad (8)$$

$$c = \frac{\left(\frac{\theta_{NO}^{1\times1}}{\theta_{NO}^{crit}} + \frac{\theta_{O}^{1\times1}}{\theta_{O}^{crit}}\right)}{\theta_{1\times1}} \quad (9)$$

where $\theta_{def}^{1\times1} = \theta_{1\times1}\theta_{def}$ and the parameter values are given in Table 1. A single adsorption site was assumed for all adsorbates so that $\theta_{NO}^{1\times1} + \theta_{NH_3}^{1\times1} + \theta_{O}^{1\times1} + \theta_{N}^{1\times1} + \theta_{H}^{1\times1} \leq \theta_{1\times1}$.

The conversion of hex to 1 × 1 takes place through NO adsorption onto the hex phase via an NO island growth mechanism, NO molecules that adsorb on the hex phase migrate to 1 × 1 patches and cause these islands to grow at the expense of the surrounding hex area. Growth of 1 × 1 islands occurs at constant local NO coverage $\theta_{grow}^{1\times1}$ and once it exceeds this critical value. All of these experimental observations were included in the model through a value of $\theta_{grow}^{1\times1} = 0.36$, obtained by fitting simulations with the experimental measurements of ref 8.

The recently proposed nonlinear dependence of the 1 × 1 ↔ hex phase transition on the NO coverage in the hex phase[10−12] was not included in this model because its inclusion implies additional mathematical difficulties that will be the subject of further work.

The phase transition 1 × 1 → hex is initiated when the coverages of NO and O on the 1 × 1 areas fall below critical values. A stabilizing effect of H_{ad} on the 1 × 1 phase exists, but it was neglected here because $\theta_{H}^{1\times1}$ is always low in the simulations.

It was assumed that there is a fraction of defect sites, θ_{def}, homogeneously distributed on the surface. Therefore, the total amount of defects in the 1 × 1 or hex phase is obtained by multiplying θ_{def} by $\theta_{1\times1}$ or θ_{hex}, respectively. Defects can either exist on the surface as scratches not directly linked to the reaction or be created during the phase transition due to the rearrangements of the platinum atoms. The last possibility implies that the concentration of defects depends on time, and we have to consider it as an additional variable in the model. Equation 7 describes the evolution of the so-called dynamic defects. In addition, we considered a small fraction of static defects, which remains constant during the reaction. The first term in eq 7 represents the creation of defects due to the phase transition, and the second term stands for defect elimination by annealing.

TABLE 1: Temperature-Independent Parameters

description	parameter	value
NO-adsorption flux 1×1, hex	F_{NO}	2.21
NH_3-adsorption flux 1×1	F_{NH_3}	2.84
H_2-adsorption flux 1×1	F_{H_2}	8.28
parameter for NO desorption activation energy	α	24 (kcal $\times$ mol^{-1})
parameter for NH_3 desorption activation energy	ϕ	30 (kcal $\times$ mol^{-1})
inhibition coverage of NO for NO dissociation	θ_{NO}^{inh}	0.61 (ML)
inhibition coverage of O for NO dissociation	θ_{O}^{inh}	0.399 (ML)
critical coverage of NO for the $1 \times 1 \rightarrow$ hex phase transf.	θ_{NO}^{crit}	0.3 (ML)
critical coverage of O for the $1 \times 1 \rightarrow$ hex phase transf.	θ_{O}^{crit}	0.4 (ML)
coverage for island growth in the hex $\rightarrow 1 \times 1$ phase transf.	$\theta_{grow}^{1\times1}$	0.36 (ML)

TABLE 2: Rate Constants for the NO + NH_3 Reaction on Pt{100}

reaction step	parameter	ν_i (s^{-1})	E_i (kcal $\times$ mol^{-1})	value at $T = 425$ K (s^{-1})
NO-desorption 1×1	k_1	1.7×10^{14}	37.0[a]	1.6×10^{-5}
NO-dissociation 1×1	k_2	2.0×10^{15}	28.5	4.4
NO-trapping on 1×1	k_3	2.2×10^{4}	8.0	1.7
NO-desorption hex	k_4	4.0×10^{12}	26.0	0.17
NH_3-desorption 1×1	k_5	1.0×10^{9}	18.0[a]	0.55
NH_3-decomposition 1×1	k_6	1.0×10^{15}	17.9	60.16
NH_3-formation 1×1	k_7	1.0×10^{10}	16.0	59.1
H_2O-formation 1×1	k_8	1.0×10^{13}	13.0	2.1×10^{6}
N_2-desorption 1×1	k_9	1.3×10^{12}	19.0	2.2×10^{2}
H_2-desorption 1×1	k_{10}	8.0×10^{12}	23.0	11.9
transition $1 \times 1 \rightarrow$ hex	k_{11}	2.5×10^{11}	25.8	1.28×10^{-2}
NO-untrapping	k_{12}	9.3×10^{5}	19.0[b]	1.52×10^{-4}
creation of defects	k_{13}	0.06	0.0	6.0×10^{-2}
annealing of defects	k_{14}	1.5×10^{14}	33.0	1.5×10^{-3}

[a] For zero local coverage, see eq 10. [b] $E_{12} = E_1 + E_3 - E_4$, see ref 13.

TABLE 3: Diffusion Energies and Constants

process	E (kJ mol^{-1})	value at 420 K (cm^2 s^{-1})
NO-diffusion (1×1)	28	3.3×10^{-7}
NO-diffusion (hex)	22	1.8×10^{-6}
NH_3-diffusion	15	1.4×10^{-5}
O-diffusion	NA[a]	always set to 0
N-diffusion	NA	always set to 0
H-diffusion	18	5.7×10^{-6}

[a] Not applicable.

We assumed that a certain fraction of defects in the 1×1 phase cannot be transformed to the hex one because the $1 \times 1 \rightarrow$ hex phase transformation terminates when $\theta_{1\times1} = \theta_{def}^{hex}$. Also, the creation of 1×1 phase proceeds while $\theta_{1\times1}$ is less than the maximum fraction of surface that can be transformed to the 1×1 phase, that is, $1 - \theta_{def}^{1\times1}$.

The temperature dependence of the rate constants $k_1, \ldots, k_{14}$ is expressed via the Arrhenius law $k_i = \nu_i e^{-E_i/RT}$, and the values are reported in Table 2. The coverage dependence of NO and NH_3 desorption energies is taken into account by

$$E_1 = E_1^0 - \alpha\left(\frac{\theta_{NO}^{1\times1}}{\theta_{1\times1}}\right)^2, \qquad E_5 = E_5^0 - \phi\left(\frac{\theta_{NH_3}^{1\times1}}{\theta_{1\times1}}\right)^2 \quad (10)$$

where α and ϕ are given in Table 1.

The kinetic behavior of the IMI model has been studied in ref 13 and compared with experimental data.

The IMI model mainly improves the dependence of the oscillatory period on temperature, compared with the former LFI model, and in the present work we show that this fact also modifies the spatiotemporal behavior predicted for the NO + NH_3 reaction.

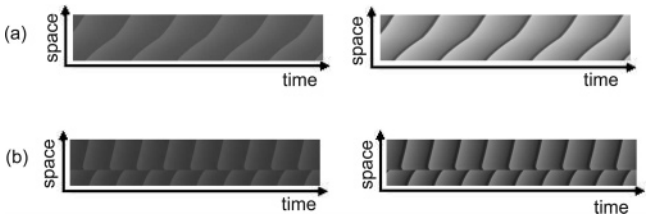

Figure 1. Space−time diagrams at (a) $T = 420$ K and (b) $T = 430$ K. Left: the gray scale is proportional to $\theta_{1\times1}$. Right: the gray scale is proportional to $\theta_{NH_3}^{1\times1}$. Periodic boundary conditions are used.

The LFI model has been spatially extended, and the formation of different kinds of patterns has been shown in 1D and 2D.[17,18] To obtain front waves as stable patterns, site-blocking effects on the diffusion of the adsorbates and fixed macroscopic surface defects had to be imposed.[19] These attempts, however, had poor success in describing the existence of propagating patterns as stable responses of the system.

In the present work, we show that the IMI model is able to reproduce front waves with Fickean diffusion coefficients. To spatially extend the model, constant diffusion coefficients are introduced, resulting in a reaction-diffusion system of the form

$$\frac{\partial x(t, q)}{\partial t} = f(x(t, q); p, T) + M(T)\nabla^2 x(t, q) \quad (11)$$

where q is the spatial variable and $M(T)$ is a temperature-dependent diagonal diffusion matrix. $f(x(t, q); p, T)$ refers to the kinetic terms of the IMI model. The diffusion constants (D_i) were calculated as in refs 17 and 18 by using the Arrhenius expression $D_i = \nu_i \exp(-E_i/RT)$, where $\nu_i = 0.001$ $cm^2 s^{-1}$ and E_i are the activation energies summarized in Table 3, R is the gas constant, and T is the absolute temperature. Note that the activation energies are those used in refs 17 and 18.

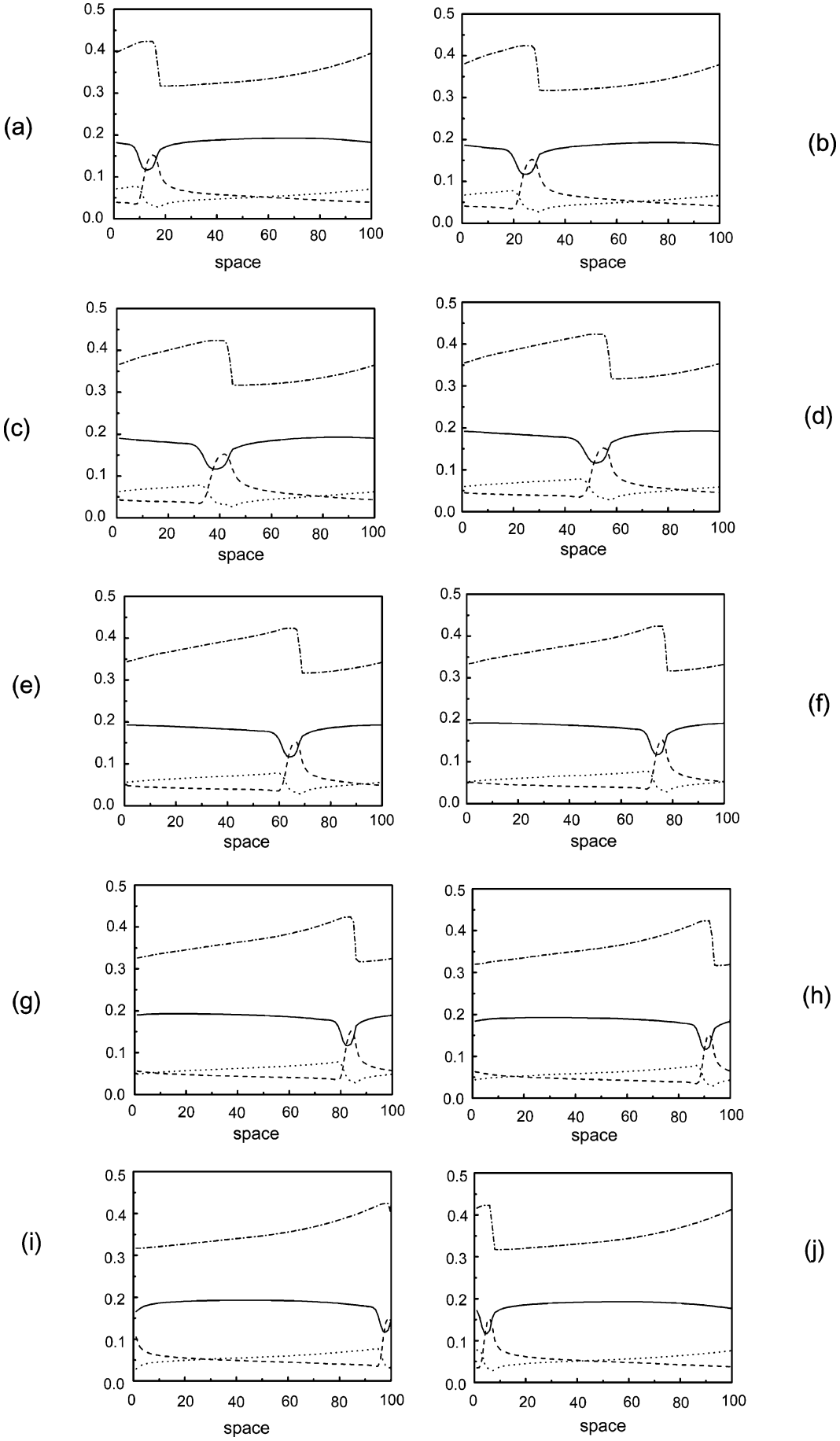

Figure 2. Concentration profiles of $\theta_{1\times1}$ (dot−dash line), θ_{NO}^{hex} (continuous line), $\theta_{NO}^{1\times1}$ (dash line), and $\theta_{NH_3}^{1\times1}$ (dot line) across the surface as a function of time and at $T = 420$ K. The time increases from a to j.

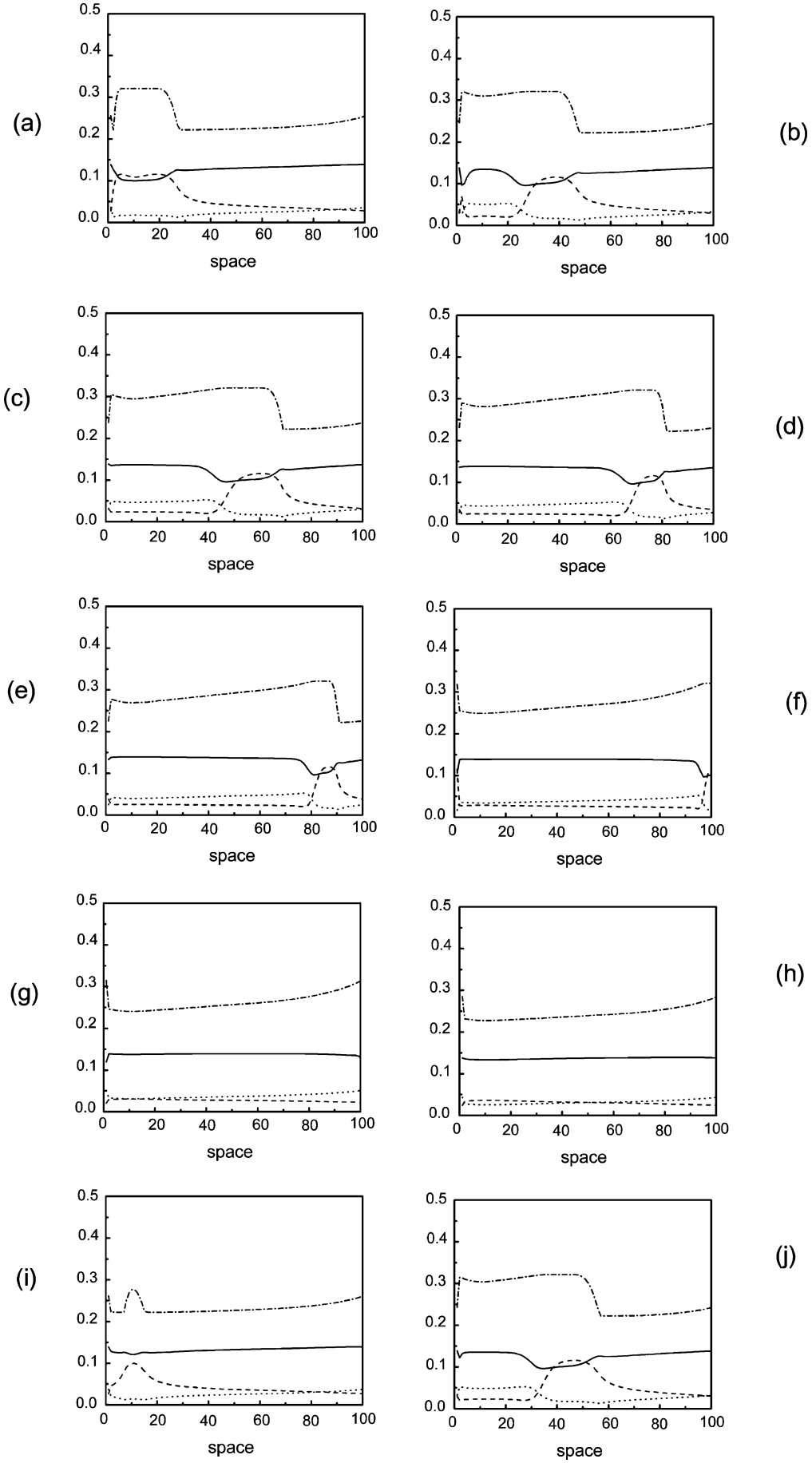

Figure 3. Concentration profiles of $\theta_{1\times1}$ (dot−dash line), θ_{NO}^{hex} (continuous line), $\theta_{NO}^{1\times1}$ (dash line), and $\theta_{NH_3}^{1\times1}$ (dot line) across the surface as a function of time and at $T = 430$ K. The time increases from a to j.

The system of eq 11 was numerically integrated in 1D in the present work by using a simple Euler scheme with $\Delta x = 0.01$ cm with periodic boundary conditions. The integration time step (Δt) was chosen in each case to ensure mathematical stability. Results were checked to be independent of the integration step for sufficiently small values of Δt.

With appropriate initial conditions, we found traveling waves in a wide range of temperature. As temperature increases, phase waves appear following a scenario similar to that observed in the extended model developed by Krischer, Eiswirth, and Ertl (KEE), for the CO oxidation on Pt{110}.[21−23] Gas global coupling has been introduced with realistic values of pumping flow (120 L/s < J < 200 L/s), and macroscopic oscillations have been observed coexisting with traveling waves in agreement with the experiments.[8] Results and conclusions are summarized in the next section.

3. Results

Simulations were started with an initial condition consisting of a linear gradient in the nondiffusive variable $\theta_{1\times1}$.

After a transient of several oscillation periods, the system reaches an asymptotic behavior with sustained traveling waves propagating across the surface.

Figure 1 shows the fronts obtained at $T = 420$ K (a) and $T = 430$ K (b). Both $\theta_{1\times1}$ and $\theta_{NH_3}^{1\times1}$ profiles are shown in each case. The reaction fronts are asymptotic stable responses of the system and *are not associated with fixed defects*.

For a better understanding of the spatiotemporal behavior shown in Figure 1, in Figures 2 and 3 we plotted (at $T = 420$ K and $T = 430$ K, respectively) the concentration profiles of $\theta_{1\times1}$, θ_{NO}^{hex}, $\theta_{NO}^{1\times1}$, and $\theta_{NH_3}^{1\times1}$ at 10 different time values (from a−j). The coordinate origin was arbitrarily shifted to the spatial point near the minimum wave velocity (see below).

As the front propagates to the right, it becomes narrower and its velocity diminishes until a new wave is generated. The effect increases with temperature and at $T = 430$ K the traveling wave almost stops and oscillations on the left disappear until a new fluctuation on the right of the wave generates a new propagating pattern.

The propagating patterns obtained at different temperatures have distinctive characteristics that can be visualized by performing a transformation to amplitude and phase variables. The procedure was first introduced by Mikhailov and co-workers to provide a formal approach to the analysis of pattern formation observed in real experimental situations or in realistic models.[24,25] The latter is the case of the present work; the oscillations in the IMI model are strongly unharmonic, as shown in Figure 4a, and the variable transformation is then referred to the limit cycle displayed by the kinetic model.

The propagating pattern characteristics, at different temperatures, are illustrated in Figures 4b and c in the projection of the limit cycle on the (θ_{NO}^{hex}, $\theta_{NO}^{1\times1}$) plane. In these figures, the continuous lines correspond to the limit cycle of the kinetic model and the symbols display the spatial evolution of the variables at the times illustrated in Figures 2 and 3. We characterize the limit cycle with a radius $\rho(t)$ and define the amplitude $R(t)$ as the relative distance of a given point of the traveling wave to the limit cycle. The phase ϕ is defined with respect to an arbitrarily chosen point of reference. The phase ϕ increases as the variables evolve in time and changes by 2π after each period.

Figure 4b shows that, at $T = 420$ K, traveling waves adopt all of the possible values of ϕ across the surface at every time; that is, ϕ changes continuously from 0 to 2π in $x \in [0, L]$ $\forall$ t.

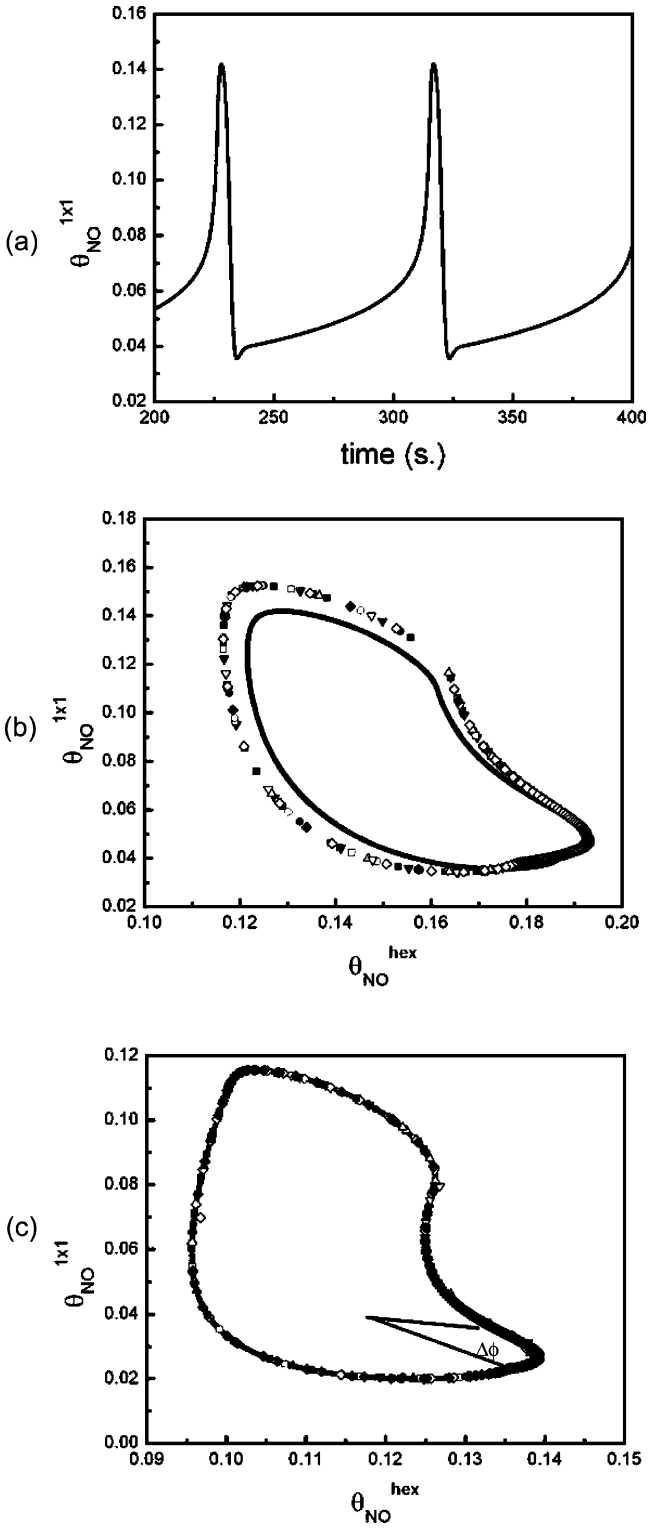

Figure 4. (a) Temporal evolution of $\theta_{NO}^{1\times1}$ in the kinetic IMI model at $T = 420$ K. (b and c) Wave patterns in the phase-space representation at $T = 420$ K (b) and $T = 430$ K (c). The continuous line represents the limit cycle of the kinetic model. Symbols display the spatial evolution of the variables at the times illustrated in Figures 2 and 3 (form a to j): filled circle, filled square, filled up-triangle, filled down-triangle, filled diamond, open circle, open square, open up-triangle, open down-triangle, open diamond. At $T = 430$ K the angle indicates the minimum interval of ϕ, displayed by the phase wave.

Also, R changes across the surface, taking a maximum value far away from the limit cycle and then returning to it. *Traveling patterns at $T = 420$ K correspond to amplitude modulations propagating across the surface.*

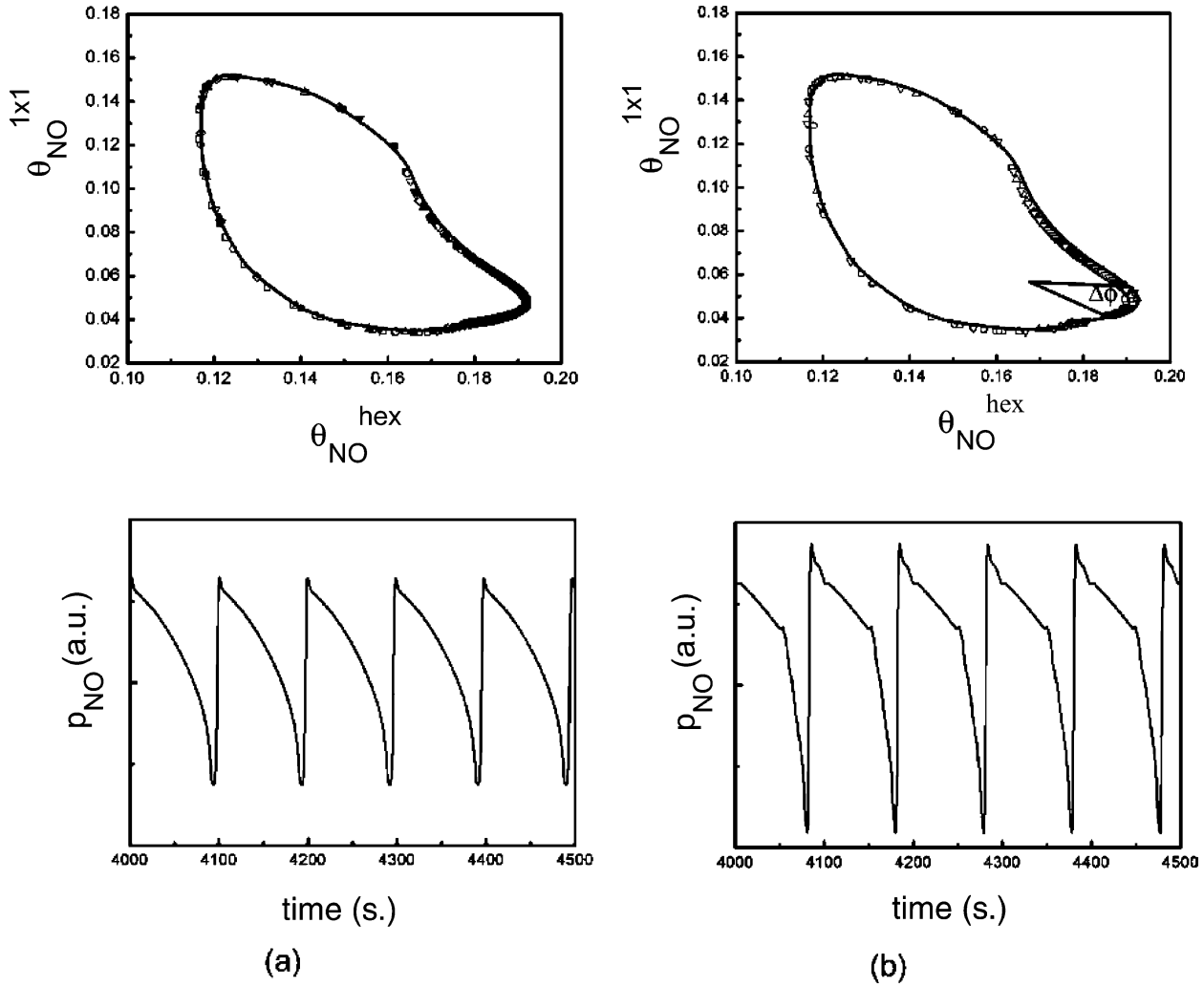

Figure 5. Wave patterns in the extended IMI model with GGC at $T = 420$ K in the phase-space representation. The continuous line represents the limit cycle of the diffusive model. (a) $\tau = 0.3$ s, (b) $\tau = 0.5$ s, the angle indicates the minimum interval of ϕ, displayed by the phase wave. Lower panels display the corresponding temporal evolution of p_{NO}.

The situation dramatically changes as T increases, and at $T = 430$ K the waves evolve on the limit cycle displayed by the kinetic model; that is, the patterns are phase waves. Referring to the frames displayed in Figure 3, we note that at the time corresponding to frame a $\phi \in [0, 2\pi]$. However, as time increases and the wave profile becomes narrow the ϕ interval also diminishes. As the wave collapses (frame h), the ϕ interval is minimum as indicated in Figure 4c.

The scenario described above has been observed previously in other reaction-difussion models with global coupling via the gas phase or delayed feedback,[21−23] but it has never been reported before in the NH_3 + NO/Pt{100} system. In the present model, the high mobility of adsorbed H is responsible for the appearance of such patterns even in the absence of coupling through the gas phase.

The behavior of the system seems to be dependent on the initial conditions, with different kinds of patterns coexisting at the same temperature. A complete phase diagram will be the subject of further work.

Gas global coupling (GGC) should shift the transition from amplitude waves to phase waves to lower temperatures.

GGC was introduced in the present work by considering the temporal variation of the partial pressures of the reactants andproducts.[25,26] In the IMI model, the GGC leads to the introduction of five additional equations that are written as

$$\frac{\mathrm{d}\,p_{NO}}{\mathrm{d}t} = K(p^0_{NO} - p_{NO}) - \alpha \int_{A_s}\{F_{NO}\,p_{NO}(\theta_{1\times1} - \theta^{1\times1}_{NO} - 4\theta^{1\times1}_{NH_3}) - k_1\theta^{1\times1}_{NO} + F_{NO}\,p_{NO}(\theta_{hex} - \theta^{hex}_{NO}) - k_4\theta^{hex}_{NO}\} \quad (12)$$

$$\frac{\mathrm{d}\,p_{NH_3}}{\mathrm{d}t} = K(p^0_{NH_3} - p_{NH_3}) - \alpha \int_{A_s}\{F_{NH_3}\,p_{NH_3}(\theta_{1\times1} - 3\theta^{1\times1}_{NH_3} - 1.6\theta^{1\times1}_{NO}) - k_5\theta^{1\times1}_{NH_3}\} \quad (13)$$

$$\frac{\mathrm{d}\,p_{N_2}}{\mathrm{d}t} = K(p^0_{N_2} - p_{N_2}) + \alpha \int_{A_s}\left\{k_9\frac{(\theta^{1\times1}_{N})^2}{\theta_{1\times1}}\right\} \quad (14)$$

$$\frac{\mathrm{d}\,p_{H_2}}{\mathrm{d}t} = K(p^0_{H_2} - p_{H_2}) + \alpha \int_{A_s}\left\{k_{10}\frac{(\theta^{1\times1}_{H})^2}{\theta_{1\times1}}\right\} \quad (15)$$

$$\frac{\mathrm{d}\,p_{H_2O}}{\mathrm{d}t} = K(p^0_{H_2O} - p_{H_2O}) + \alpha \int_{A_s}\left\{k_8\frac{\theta^{1\times1}_{O}\,\theta^{1\times1}_{H}}{\theta_{1\times1}}\right\} \quad (16)$$

where p^0_i are the initial partial pressure of the ith species and $p^0_{N_2} = p^0_{H_2} = p^0_{H_2O} = 0$, $K = J/V$ is the pumping rate with J as the pumping flux and V as the volume of the chamber. The

pumping rate can be written as $K = 1/\tau$, where τ is a relaxation time. Realistic values of $J \approx 160$ L/s and $V \approx 60$ L yield to $\tau \approx 0.37$ s. In practice, we used τ as an adjustable parameter to vary the GGC strength, which is equivalent to experimentally modifying the pumping flux intensity 120 L/s $\leq J \leq$ 200 L/s.

The H_2 adsorption has not been included because p_{H_2} remains low during simulations. In eqs 12−16, α is the GGC constant and is written as

$$\alpha = \alpha_0 \frac{A_c}{A_s} \tag{17}$$

where A_c is the crystal area that contributes as a whole to the gas global coupling, whereas A_s is the simulated area, which is normally much less of the real crystal area and, in the present case, corresponds to a strip of about 100 μm^2, and α_0 is

$$\alpha_0 = 1.379 \times 10^{-19} \frac{N_0 T}{V} \tag{18}$$

where $N_0 = 2 \times 10^{15}$ is the number of adsorption sites per square centimeter, T is the absolute temperature, and V is the volume of the chamber.

Figure 5 shows the patterns obtained at $T = 420$ K in the phase-space representation and at two different values of τ. Propagating waves always evolve on the limit cycle displayed by the diffusive system (Figure 4b), which is then used to define the amplitude variable $R(t)$. In this case, $R(t)$ is constant and equal to one. GGC has the effect of concentrating the phase of the pattern. At $\tau = 0.3$ s, waves propagate on the surface adopting all of the possible values of ϕ across the surface at every time; that is, ϕ changes continuously from 0 to 2π in $x \in [0, L] \; \forall \; t$. Because these patterns are still analogous to those shown in Figure 4b, we shall call them amplitude waves (though $R(t)$ is constant). At $\tau = 0.5$ s, the wave phase gradually concentrates, and, at a given time, the ϕ interval reaches a minimum value on the surface as indicated in Figure 5b. These patterns are phase waves. Therefore, the transition from amplitude to phase waves occurs at a given temperature by increasing the gas global coupling (i.e., increasing τ).

Propagating waves coexist with macroscopic oscillations in the partial pressures of the reactants, which are more pronounced as the strength of the GGC increases. This fact is in agreement with the experimental information,[6−8] where after a state dominated by targets and without oscillations in the partial pressures, an increase in temperature (and therefore in GGC) makes macroscopic oscillations emerge with still observable traveling fronts on the surface. At higher temperatures, GGC induces island formation and homogeneous oscillations of the surface as a whole, but this regime will be discussed in further work.

4. Conclusions

In the present work, we simulated the existence of traveling waves in the NO + NH_3 reaction on Pt{100} by spatially extending the IMI model with Fickean diffusion and global gas-phase coupling. A transition from amplitude to phase waves was found to be induced either by temperature or by gas global coupling. Although in other reaction-diffusion systems such as CO + O_2 on Pt{110} this transition was observed to be only induced by GGC or delayed feedback, the IMI model predicts it in a surface reaction coupled only by diffusion. We argue that the difference is due to the existence of highly mobile species such as adsorbed hydrogen.

The traveling waves simulated in the present work are stable asymptotic responses of the system (though seem to be dependent on the initial condition) and *are not associated with fixed defects*. This fact is in agreement with previous experimental studies on such reaction reporting evidence of the existence of spiral centers capable of moving on the surface.[20] Also, the IMI model adequately predicts the coexistence of macroscopic oscillations in the partial pressures of the reactants and front wave patterns on the surface.

Acknowledgment. This work was supported by Consejo de Investigaciones Científicas y Técnicas (CONICET), Comisión de Investigaciones Científicas de la Provincia de Buenos Aires (CIC), Agencia Nacional de Promoción Científica y Tecnológica (ANPCyT), and Universidad Nacional de La Plata (UNLP).

References and Notes

(1) Egelhoff, W. F., Jr. In *The Chemical Physics of Solid Surfaces and Heterogeneous Catalysis*; King, D. A., Woodruff, D. P., Eds.; Elsevier, Amsterdam; Vol. 4, 1982.
(2) Shelef, M. *Catal. Rev. Sci. Eng.* **1975**, 11.
(3) Lombardo, S. J.; Fink, T.; Imbihl, R. *J. Chem. Phys.* **1993**, *98*, 5526.
(4) Takoudis, C. G.; Schmidt, L. D. *J. Phys. Chem.* **1983**, *87*, 958.
(5) Katona, T.; Somorjai, G. A. *J. Phys. Chem.* **1992**, *96*, 5465.
(6) Lombardo, S. J.; Esch, F.; Imbihl, R. *Surf. Sci.* **1992**, *271*, L367.
(7) Lombardo, S. J.; Slinko, M.; Fink, T.; Löher, T.; Madden, H. H.; Imbihl, R.; Esch, F.; Ertl, G. *Surf. Sci.* **1992**, *269/270*, 481.
(8) Veser, G.; Esch, F.; Imbihl, R. *Catal. Lett.* **1993**, *13*, 371.
(9) Bradley, J. M.; Pasteur, A. T.; King, D. A. *J. Chem. Soc., Faraday Trans.* **1996**, *92*, 2941.
(10) Bradley, J. M.; Hopkinson, A.; King, D. A. *Surf. Sci.* **1997**, *371*, 255.
(11) Walker, A. V.; Gruyters, M.; King, D. A. *Surf. Sci. Lett.* **1997**, *384*, L791.
(12) Gruyters, M; Pasteur, A. T.; King, D. A. *J. Chem. Soc., Faraday Trans.* **1996**, *92*, 2941.
(13) Irurzun, I. M.; Mola, E. E.; Imbihl, R. *Chem. Phys.* **2006**, *323*, 295.
(14) Scheibe, A.; Lins, U.; Imbihl, R. *Surf. Sci.* **2005**, *577*, 1.
(15) Schultz, E.; Imbihl, R. *Z. Phys. Chem.* **2002**, *216*, 509.
(16) Uecker, H; Imbihl, R.; Rafti, M; Irurzun, I. M.; Vicente, J. L.; Mola, E. E. *Chem. Phys. Lett* **2003**, *382*, 232.
(17) Uecker, H. *Physica D* **2003**, *190*, 249.
(18) Uecker, H. *Phys. Rev. E* **2005**, *71*, 016207.
(19) Rafti, M.; Vicente, J. L.; Uecker, H.; Imbihl, R. *Chem. Phys. Lett.* **2006**, *421*, 577.
(20) Irurzun, I. M.; Imbihl, R.; Vicente, J. L.; Mola, E. E. *Chem. Phys. Lett.* **2004**, *389*, 212.
(21) Krischer, K.; Eiswirth, M.; Erlt, G. *J. Chem. Phys.* **1992**, *96*, 9161.
(22) Bertram, M. Ph.D. Thesis, Technische Universitat Berlin, 2002.
(23) Bertram M.; Mikhailov, A. S. *Phys. Rev. E* **2001**, *63*, 066102.
(24) Bertram M.; Mikhailov, A. S. *Phys. Rev. E* **2003**, *67*, 036207.
(25) Bertram, M; Beta, C.; Pollmann, M.; Mikhailov, A. S.; Rotermund, H. H.; Ertl, G. *Phys. Rev. E* **2003**, *67*, 036208.
(26) von Oertzen, A.; Rotermund, H. H.; Mikhailov, A. S.; Erlt, G. *J. Phys. Chem. B* **2000**, *104*, 3155.